Supplementary Note 1

The diffusion process of guest molecules inside a nanoporous slab is described by[1, 2]

$$\frac{\partial C}{\partial t} = D\frac{\partial^2 C}{\partial x^2}, \qquad \text{(Supplementary Equation 1)}$$

where C is the concentration of guest molecules in intracrystalline space, t the uptake/release time, D the intracrystalline (transport) diffusivity, and x the Cartesian coordinate. The boundary conditions can be described with two dimensionless variables $\eta = x/l$ and $\tau = Dt/l^2$:

$$\frac{\partial C}{\partial \eta}|_{\eta=0} = 0, \qquad \text{(Supplementary Equation 2)}$$

$$\frac{\partial C}{\partial \eta}|_{\eta=1} = L\left(C_{\mathrm{eq}} - C|_{\eta=1}\right), \qquad \text{(Supplementary Equation 3)}$$

where $L = (\alpha l)/D$ is the ratio of the characteristic time of intracrystalline diffusion to that of surface barriers, α the surface permeability, C_{eq} the concentration of guest molecules in equilibrium with the external gas pressure, and l the half thickness of the plane sheet.

The initial condition of Supplementary Equation 1 is shown below,

$$C|_{\tau=0} = 0. \qquad \text{(Supplementary Equation 4)}$$

By applying Laplace transform to Supplementary Equation 1, the intracrystalline concentration C of guest molecules can be solved,

$$\frac{C}{C_{\mathrm{eq}}} = \mathrm{erfc}\left(\frac{1-\eta}{2\sqrt{\tau}}\right) - \exp(L(1-\eta) + L^2\tau)\mathrm{erfc}\left(L\sqrt{\tau} + \frac{1-\eta}{2\sqrt{\tau}}\right) + \mathrm{erfc}\left(\frac{1+\eta}{2\sqrt{\tau}}\right) - \exp(L(1+\eta) + L^2\tau)\mathrm{erfc}\left(L\sqrt{\tau} + \frac{1+\eta}{2\sqrt{\tau}}\right) + \cdots. \qquad \text{(Supplementary Equation 5)}$$

And the accumulation rate of mass of guest molecules in the half slab can be represented as

$$\frac{\mathrm{d}\left(\frac{m_t}{MV}\right)}{\mathrm{d}\tau} = \frac{\partial C}{\partial \eta} = L\left(C_{\mathrm{eq}} - C|_{\eta=1}\right), \qquad \text{(Supplementary Equation 6)}$$

where m_t is the total absorbed quantity of guest molecules at time t for the half slab, M the molar mass of guest molecules, and V the volume of the half slab model.

Integrating Supplementary Equation 6 with variable τ, we have

$$\frac{m_t}{MV} = \int_0^\tau L\left(C_{\mathrm{eq}} - C|_{\eta=1}\right)\mathrm{d}\tau. \qquad \text{(Supplementary Equation 7)}$$

According to the Supplementary Equation 5, when $\eta = 1$ we can write C as

$$C\ |_{\eta=1} = C_{\mathrm{eq}}\left[1 - \exp(L^2\tau)\mathrm{erfc}\left(L\sqrt{\tau}\right) + \mathrm{erfc}\left(\frac{1}{\sqrt{\tau}}\right) - \exp(2L + L^2\tau)\mathrm{erfc}\left(L\sqrt{\tau} + \frac{2}{\sqrt{\tau}}\right) + \cdots\right]. \quad \text{(Supplementary Equation 8)}$$

The Supplementary Equation 8 can be further simplified when τ approaches 0,

$$C\ |_{\eta=1}^{\tau\to 0} = C_{\mathrm{eq}}\left[1 - \exp(L^2\tau)\mathrm{erfc}\left(L\sqrt{\tau}\right)\right]. \quad \text{(Supplementary Equation 9)}$$

Therefore, for a short time, the Supplementary Equation 7 can be written as

$$\frac{m_t}{MV}\ |^{\tau\to 0} = LC_{\mathrm{eq}}\int_0^{\tau}\left(\exp(L^2\tau)\mathrm{erfc}\left(L\sqrt{\tau}\right)\right)\mathrm{d}\tau. \quad \text{(Supplementary Equation 10)}$$

Note that

$$\int_0^{\tau}\left(\exp(L^2\tau)\mathrm{erfc}\left(L\sqrt{\tau}\right)\right)\mathrm{d}\tau = \frac{1}{L^2}\left[\exp(L^2\tau)\mathrm{erfc}\left(L\sqrt{\tau}\right)\right]\ |_0^{\tau} -$$

$$\frac{1}{L^2}\int_0^{\tau}\left(\frac{2}{\sqrt{\pi}}\exp(L^2\tau)\left(-\exp(-L^2\tau)\frac{L}{2\sqrt{\tau}}\right)\right)\mathrm{d}\tau, \quad \text{(Supplementary Equation 11)}$$

it can be simplified to

$$\int_0^{\tau}\left(\exp(L^2\tau)\mathrm{erfc}\left(L\sqrt{\tau}\right)\right)\mathrm{d}\tau = \frac{1}{L^2}\left[\exp(L^2\tau)\mathrm{erfc}\left(L\sqrt{\tau}\right) - 1 + L\int_0^{\tau}\left(\frac{1}{\sqrt{\pi\tau}}\right)\mathrm{d}\tau\right]$$

(Supplementary Equation 12)

or

$$\int_0^{\tau}\left(\exp(L^2\tau)\mathrm{erfc}\left(L\sqrt{\tau}\right)\right)\mathrm{d}\tau = \frac{1}{L^2}\left[\exp(L^2\tau)\mathrm{erfc}\left(L\sqrt{\tau}\right) - 1 + L\frac{2\sqrt{\tau}}{\sqrt{\pi}}\right].$$

(Supplementary Equation 13)

Thus, the Supplementary Equation 10 becomes

$$\frac{m_t}{MV}\ |^{\tau\to 0} = C_{\mathrm{eq}}\left[\sqrt{\frac{4\tau}{\pi}} - \frac{1-\exp(L^2\tau)\mathrm{erfc}\left(L\sqrt{\tau}\right)}{L}\right]. \quad \text{(Supplementary Equation 14)}$$

Note that m_∞ represents the total mass of guest molecules adsorbed for a half slab of porous material after reaching the equilibrium state, we have

$$\frac{m_\infty}{MV} = C_{\mathrm{eq}}. \quad \text{(Supplementary Equation 15)}$$

When t approaches 0, the relative loading of guest molecules at the initial stage can be reduced to[3]

$$\frac{m_t}{m_\infty}\ |^{t\to 0} = \sqrt{\frac{4Dt}{\pi l^2}} - \frac{1-\exp\left(L^2\frac{D}{l^2}t\right)\mathrm{erfc}\left(L\sqrt{\frac{Dt}{l^2}}\right)}{L},$$

(Supplementary Equation 16)

where m_t/m_∞ is the relative uptake loading of guest molecules.

Defining a function

$$f\left(\sqrt{t}\right) = \sqrt{\frac{4D}{\pi l^2}}\sqrt{t} - \frac{1-\exp\left(L^2\frac{D}{l^2}\left(\sqrt{t}\right)^2\right)\mathrm{erfc}\left(L\sqrt{\frac{D}{l^2}}\sqrt{t}\right)}{L},$$

(Supplementary Equation 17)

we can expand the Supplementary Equation 17by Taylor series of variable $\sqrt{t}$,

$$f\left(\sqrt{t}\right) \cong f(0) + f^{(1)}(0)\sqrt{t} + \frac{f^{(2)}(0)}{2!}\left(\sqrt{t}\right)^2 + O\left(\left(\sqrt{t}\right)^3\right),$$

(Supplementary Equation 18)

where

$$f(0) = \sqrt{\frac{4D}{\pi l^2}}\cdot 0 - \frac{1-\exp\left(\frac{L^2D}{l^2}\cdot 0^2\right)\mathrm{erfc}\left(L\sqrt{\frac{D}{l^2}}\cdot 0\right)}{L} = 0,$$

(Supplementary Equation 19)

$$f^{(1)}(0) = \frac{\mathrm{d}f\left(\sqrt{t}\right)}{\mathrm{d}\sqrt{t}}\Big|^{\sqrt{t}\to 0} = \sqrt{\frac{4D}{\pi l^2}} + \frac{L\sqrt{D/l^2}\left(-2/\sqrt{\pi}\right)}{L} = 0,$$

(Supplementary Equation 20)

$$f^{(2)}(0) = \frac{\mathrm{d}^2 f\left(\sqrt{t}\right)}{\mathrm{d}\sqrt{t}^2}\Big|^{\sqrt{t}\to 0} = \frac{2\alpha}{l}.$$

(Supplementary Equation 21)

Then we can obtain the relation between relative loading of guest molecules at initial uptake stage as a function of $\sqrt{t}$,

$$\frac{m_t}{m_\infty}\Big|^{\sqrt{t}\to 0} \cong \frac{\alpha}{l}\left(\sqrt{t}\right)^2 + O\left(\sqrt{t}^3\right).$$

(Supplementary Equation 22)

The Supplementary Equation 22 reveals that at the initial uptake stage the relative loading of guest molecules is a quadratic function of $\sqrt{t}$. By use of the Supplementary Equation 22, we could conveniently determine the surface permeability α with characteristic intracrystalline length of intracrystalline diffusion l.

Supplementary Note 2

Supplementary Figure 22 shows the fitting of the initial uptake curve (plotted as a function of the square root of time) by equation (3) with different time interval. As can be seen, the fitting results are not sensitive to the selected time intervals. In Supplementary Table 10, the surface permeability determined by equation (3) has relatively low uncertainty, and the intracrystalline diffusivity calculated via DRM with known surface permeability shows a small fluctuation and is within a narrow range. By use of the method with both intracrystalline diffusivity and surface permeability as free parameters in DRM, however, a high uncertainty of fitting results can be observed (see Supplementary Table 11).

Supplementary Note 3

We note that a crucial parameter in DRM is the characteristic factor L ($=\alpha l/D$). The characteristic factor L can reflect the significance of intracrystalline diffusion over surface barriers in mass transfer of guest molecules. A large L means that the intracrystalline diffusion dominates the mass transfer, while a small L reveals the dominance of surface barriers in mass transfer.

In order to study the application range of equation (3) in quantifying surface barriers, we have conducted an analysis on the uptake rates with different L by use of DRM (*i.e.* equation (1)). The parameters used in this analysis are: $l = 3\ \mu$m, $D = 1 \times 10^{-15}$ m^2/s and α = (10, 8, 4, 2, 1, 0.25, 0.0625 or 0.015625) $\times$ 10^{-8} m/s. Generally, the temporal resolution of apparatuses used in uptake rate measurement can reach the order of 1 s. For example, the time interval of data sampling is 0.5 s for TA instruments[4], 1 s for IGA (intelligent gravimetric analyzer), 0.5 s for TEOM[5] (tapered element oscillating microbalance) and 1 s for IR (infrared) spectroscopy. Therefore, the temporal resolution of data sampling is assumed to be 0.5 s in this analysis. Supplementary Figure 1 depicts the uptake rate calculated by DRM with various L (300, 240, 120, 60, 30, 7.5, 1.875, 0.46875).

As can be seen from Supplementary Figure 1a, when the intracrystalline diffusion dominates the mass transfer in nanoporous materials (*i.e.* $L > 120$)[6], the characteristic region of surface barriers, *i.e.* the *S*-shape of the initial uptake curves when plotted as a function of $t^{1/2}$, is indistinctive. It means that, for $L > 120$, equation (3) cannot be used to derive the reliable surface permeability of guest molecules based on the data obtained with common-used apparatuses such as TA, IGA. TEOM and IR spectroscopy since the temporal resolution is not low enough. In fact, as shown in Supplementary Figure 1a, it is reasonable to assume that the mass transfer is dominated by intracrystalline diffusion and surface barriers play a negligible role for $L > 120$.

When L is lower than 120, the characteristic region of the uptake curve at initial stage, which reflects the effects of surface barriers, become more pronounced. In this case, as shown in Supplementary Figure 1b, the surface permeability calculated by the equation (3) could fit the DRM very well. Note that for $L < 120$ the temporal resolution for the

uptake rate measurement is in the order of 1 s, which could meet the requirements in most of practical applications.

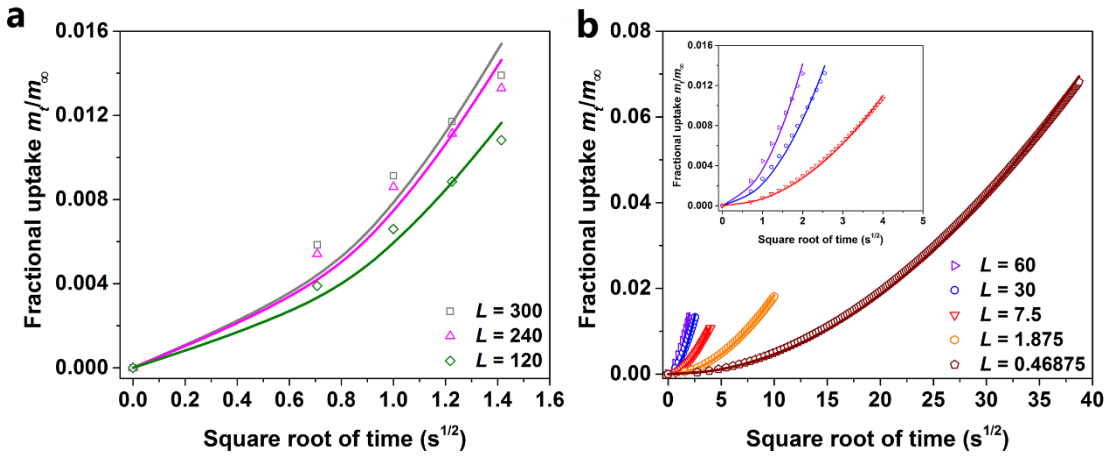

Supplementary Figure 1. Analysis based on DRM to determine the application range of equation (3). Initial uptake rates by DRM for (**a**) L = 300, 240 and 120; and (**b**) L = 60, 30, 7.5, 1.875 and 0.46875. The solid lines are fitting results by equation (3). The temporal resolution of data (scatters) sampling is 0.5 s in (a) and (b).

Supplementary Note 4

In practical applications, uptake rate measurements are usually performed with a bed of crystals. The crystals in the beds may have different crystal sizes and surface permeability for a given guest molecule[7]. Though the derivation of equation (3) is based on the uptake process for a single crystal, it can be further extended to a bed of crystals.

For any single crystal *i*, the initial uptake process can be described as

$$\frac{m_{t,i}}{m_{\infty,i}} \cong \frac{\alpha_i}{l_i}\left(\sqrt{t}\right)^2. \qquad \text{(Supplementary Equation 23)}$$

Then the initial uptake load of a bed of crystals is

$$m_t = \sum_i^n m_{t,i} \cong \sum_i^n m_{\infty,i}\frac{\alpha_i}{l_i}\left(\sqrt{t}\right)^2,$$

(Supplementary Equation 24)

where *n* represents the number of crystals in the bed. The relative uptake loading for a bed of crystals can be represented as

$$\frac{m_t}{m_\infty} \cong \frac{\sum_i^n m_{\infty,i}\frac{\alpha_i}{l_i}\left(\sqrt{t}\right)^2}{m_\infty}. \qquad \text{(Supplementary Equation 25)}$$

Note that $m_{\infty,i}$ and m_∞ are the total mass of guest molecules adsorbed in individual crystal *i* and the bed of crystals at the equilibrium state,

$$m_{\infty,i} = C_{\mathrm{eq},i}MV_i;\ m_\infty = \sum_i^n m_{\infty,i}.$$

(Supplementary Equation 26)

The Supplementary Equation 25 can be rewritten as

$$\frac{m_t}{m_\infty} \cong \frac{\sum_i^n C_{\mathrm{eq},i}V_i\frac{\alpha_i}{l_i}}{\sum_i^n C_{\mathrm{eq},i}V_i}\left(\sqrt{t}\right)^2. \qquad \text{(Supplementary Equation 27)}$$

Assuming that each crystal has same equilibrium concentration of guest molecules (*i.e.* $C_{\mathrm{eq},i} = C_{\mathrm{eq}}$), we can rewrite the Supplementary Equation 27 as

$$\frac{m_t}{m_\infty} \cong \sum_i^n \left(\frac{\omega_i}{l_i}\alpha_i\right)\left(\sqrt{t}\right)^2, \qquad \text{(Supplementary Equation 28)}$$

where $\omega_i = V_i/\sum_i^n V_i$ is the volume fraction of crystals with corresponding length l_i.

It should be noted that the derivation of the Supplementary Equation 28 is based on the assumption that all crystals in the bed have same equilibrium concentration of guest molecules. By comparing the equation (3) with the Supplementary Equation 28, we can find that the surface permeability of a bed of crystals determined by equation (3) is an

average surface permeability of diverse crystals. In this study, through the controlling of synthesis procedures and conditions as well as physical sieving[5, 7], we actually have tried to obtain samples with a narrow crystal size distribution. We agree that this possesses another limitation for our proposed method. If the bed of crystals has a wide size distribution, it is necessary to obtain particle size distribution (PSD) when using the Supplementary Equation 28. The establishment of a relation of surface permeability between individual crystal and a bed of crystals is subject to a further investigation.

Supplementary Methods

Synthesis of the SAPO-34 zeolites. The synthesis procedure of SAPO-34 zeolites used in the experiments was reported in our previous works, including SAPO-34-0.05[8], SAPO-34-0.5[9], SAPO-34-1.0 (Si-0.05)[9], SAPO-34-1.0 (Si-0.08)[9], SAPO-34-1.0 (Si-0.10)[9], SAPO-34-1.0 (Si-0.16)[9], SAPO-34-3.5[9] and SAPO-34-8[10]. The SAPO-34-8-C was purchased from Chia Tai Energy Material Ltd.

X-ray diffraction (XRD). The crystalline and phase purity of the samples were characterized by powder X-ray diffraction on a PANalytical X'Pert PRO X-ray diffractometer. Cu Kα radiation (λ = 0.154059 nm) was used as the X-ray source, operated at 40 mA and 40 kV. XRD patterns were recorded in the range of $2\theta = 5 \sim 40°$. Supplementary Figures 2 and 3 show the XRD patterns for pristine SAPO-34 zeolites with varying crystal sizes and SAPO-34-1.0 (Si-0.10) exposed to air for different time, respectively. The diffraction lines coincide with the **CHA** topology, and all samples are free from impurity phases. As shown in Supplementary Figure 3, after exposing to humid air, the crystallinity of samples, as monitored by XRD, only changes slightly. The changes of crystallinity is calculated based on the intensity of 9.5°, 21° and 31° in XRD.

Field-emission scanning electron microscopy (FE-SEM). The morphologies and crystal sizes of SAPO-34 zeolites were observed by FE-SEM Hitachi SU8020. Supplementary Figure 4 shows the FE-SEM images. SAPO-34 zeolites of different crystal size, expect SAPO-34-0.05, exhibit a similar cubic morphology. The SAPO-34-0.5 samples have an average crystal size of ~ 0.5 μm, SAPO-34-1.0 (Si-0.05) of ~ 1 μm, SAPO-34-1.0 (Si-0.08) of ~ 1 μm, SAPO-34-1.0 (Si-0.10) of ~ 1 μm, SAPO-34-1.0 (Si-0.16) of ~ 1 μm, SAPO-34-3.5 of ~ 3.5 μm, SAPO-34-8 of ~ 8 μm and SAPO-34-8-C of ~ 8 μm. The SAPO-34-0.05 samples form tiny aggregates of cubic nanocrystals, with primary crystal size from 0.03 to 0.05 μm.

X-ray fluorescence (XRF) spectrometer. The chemical composition of integral SAPO-34 zeolites was determined with a Philips Magix-601 spectrometer. As shown in Supplementary Table 1, the composition of SAPO-34 zeolites are expressed as $(Si_xAl_yP_z)O_2$, where x, y, z represent the mole fractions of silicon, aluminum and phosphorous, respectively, with $x + y + z = 1$.

Energy dispersive X-ray spectroscopy (EDX). The chemical composition of individual SAPO-34 crystals was measured by a FE-SEM Hitachi SU8020 equipped with a Horiba X-max silicon drift X-ray detector operated at an acceleration voltage of 20 kV. Supplementary Figure 5 displays the calculated atomic percentages of SAPO-34 zeolites (mainly for Si, Al and P) based on the EDX analyses. It can be observed that the Si/(Si + Al + P) ratio is consistent with the chemical composition measured by XRF (Supplementary Table 1). Furthermore, the chemical composition is more uniform inside the SAPO-34 crystals than at the crystal surface, as the value of Si/ (Si + Al + P) at crystal surface is relative higher than that inside the crystals.

Uptake rate measurement. The uptake rate measurements were carried out by use of the Intelligent Gravimetric Analyzer (IGA-100, Hiden Analytical). Specially, in order to enhance the permeability of probe gas or vapor to samples, homemade mesh type of sample cell was used. About 30 mg SAPO-34 zeolites were added to the chamber, and outgassed until a constant weight was achieved at pressure of 10^{-6} mbar and temperature of 623 K for at least 6 h. Then a steam of probe vapor was introduced into the system with a carefully controlling quantity in order to ensure the isobaric and isothermal process. Meanwhile, mass change with buoyancy corrections, system pressure and sample temperature were recorded in real-time. It should be emphasized that the effect of external or film diffusion was eliminated by changing the quantity of samples[11, 12]. To ensure the measurements exclude the influence of external diffusion, detailed results are shown in Supplementary Figure 8. The uptake curves of methanol in SAPO-34-8-C at 303 K (0 → 0.6 mbar) is shown in Supplementary Figure 9. The uptake curves of propane at 313 K (0 → 9 mbar) in pristine SAPO-34 zeolites with varying crystal sizes

and Si content are shown in Supplementary Figure 12. The uptake curves of ethane and propylene at 313 K (0 → 10 mbar) in pristine SAPO-34 zeolites are shown in Supplementary Figure 13. The uptake curves of propane at 313 K (0 → 9 mbar) in SAPO-34-1.0 (Si-0.10) exposed to different quantity of adsorbed-water and humid air (298 K) for different time are shown in Supplementary Figure 15.

Adsorption isotherms of methanol, ethane, propylene and propane were obtained using the IGA technique, in which the quantity of water adsorbed was measured by monitoring the sample weight. The adsorption isotherms are shown in Supplementary Figure 14. Under low pressure, the adsorption isotherms were fitted to the Henry's law:

$$m_\infty(p) = Kp \qquad \text{(Supplementary Equation 29)}$$

where p is the gas-phase equilibrium pressure (mbar), $m_\infty(p)$ the total mass of guest molecules adsorbed at the equilibrium state under corresponding pressure (mmol/$g_{cat.}$), and K the Henry's constant (mol·bar^{-1}·$g_{cat.}^{-1}$).

Pulsed Field Gradient Nuclear Magnetic Resonance (PFG NMR) diffusion measurement. The intracrystalline self-diffusivity of methanol in SAPO-34 zeolites at 303 K was studied with ^{1}H PFG NMR by use of a Bruker Avance III 600 spectrometer equipped with a uniaxial field gradient coils (Bruker diff50 diffusion probe) and a maximum magnetic field gradient strength of 1800 G/cm in the z-direction. The principle of PFG NMR was reported in detail elsewhere[2, 13]. Prior to ^{1}H PFG NMR tests, 202.8 mg of samples was pretreated at 673 K in a vacuum system to completely remove absorbed water and then transferred into 5 mm NMR tube (Wilmad-LabGlass) in glove box. Then methanol of ≥ 99.5% purity was introduced into the NMR tube on a homemade uptake apparatus and the loading of methanol in SAPO-34 zeolites was quantified about 0.47 mmol/$g_{cat.}$. A stimulated echo sequence with bipolar-gradient (13-interval sequence, PGSTEBP) was applied to avoid the effects of internal magnetic field gradients in the porous materials. By linearly increasing the gradient strength g in 16 steps, the spin-echo attenuation I/I_0 could be obtained with gradient duration δ and the diffusion time Δ being constant. The intracrystalline self-diffusivity D^{self} can then

be calculated by fitting the decay of the signal amplitude of the stimulated echo with the Stejskal-Tanner equation[2]:

$$I = I_0 \exp\left[-(\gamma\delta g)^2 D^{\text{self}}\left(\Delta - \frac{\delta}{3}\right)\right]$$

(Supplementary Equation 30)

where I and I_0 are the signal amplitude with and without the effect of gradient field g, respectively, γ the gyromagnetic ratio of the ^{1}H nucleus, δ the effective gradient pulse duration, g the gradient strength, D^{self} the intracrystalline self-diffusivity, and Δ the diffusion time. The results of ^{1}H PFG NMR spin-echo attenuation I/I_0 as a function of $\gamma^2\delta^2g^2(\Delta-\delta/3)$ are shown in Supplementary Figure 11.

It should be mentioned that , at sufficiently low molecular loading in zeolites, the guest molecules do not 'feel' each other, and the drag effect of guest molecules is therefore excepted to be negligible in comparison with the drag effect of host materials[14, 15]. Hence, at small molecular loading in zeolites, the intracrystalline self- and transport diffusivity could be comparable.

Pyridine-adsorbed Fourier transform infrared (FT-IR) spectra. Fourier transform infrared (FT-IR) spectra after pyridine adsorption were obtained by a Bruker Tensor 27 instrument with a resolution of 4 cm^{-1}. The calcined SAPO-34 zeolites were pressed into a self-supporting wafer (0.65 cm radius). The samples were dehydrated at 723 K for 1 h under a vacuum of 10^{-2} Pa in an IR cell, following with the acquisition of IR spectra at room temperature. Then pure pyridine vapor was adsorbed at room temperature for 5 min. After reaching equilibrium, the pyridine-absorbed system was evacuated at 423 K, and the IR spectra was acquired at room temperature. Spectra were recorded in 1000-4000 cm^{-1} range at 4cm^{-1} resolution. Pyridine (5.3 Å in diameter) was employed to evaluate acid sites situated exclusively on the external surface, as this probe molecule cannot access the micropores of the **CHA** structure (3.8 × 3.8 Å). Therefore, the quantity of pyridine adsorbed is associated with acid sites on the external surface of SAPO-34 zeolites[16]. The quantity of Brønsted acid sites (BAS) and Lewis acid sites (LAS) were calculated from the integrated absorbance (*IA*) values[17] of the

difference spectra at 1545 and 1455 cm^{-1}, respectively, based on the extinction coefficients reported by Emeis[18]. Assuming that one molecule of pyridine is adsorbed on one acid site, we can calculate *n* (external BAS) and *n* (external LAS),

$$n(\text{external BAS}) = 1.88\frac{IA(\text{B})\cdot r^2}{W_{\text{cat.}}},$$

(Supplementary Equation 31)

$$n(\text{external LAS}) = 1.42\frac{IA(\text{L})\cdot r^2}{W_{\text{cat.}}},$$

(Supplementary Equation 32)

where *IA* (B or L) is the integrated absorbance of the Brønsted and Lewis band (cm^{-1}), *r* the radius of sample wafer (cm), and $W_{cat.}$ the mass of sample wafer (mg). The detailed FT-IR of pyridine adsorbed in SAPO-34 at external surface is shown in Supplementary Figure 19-20. The quantitative results are listed in Supplementary Table 3.

Nitrogen adsorption-desorption. The nitrogen adsorption-desorption was conducted with Micromeritics ASAP 2020 at 77 K after the sample was degassed at 623 K under vacuum for 6 h. As illustrated in Supplementary Figure 21, the adsorption-desorption isotherms have step uptakes near $P/P_0 = 0$ due to the microporous structure. Typical type I isotherms for microporous materials are observed for all SAPO-34 zeolites except SAPO-34-0.05. As observed, the isotherms of SAPO-34-0.05 show the feature of type IV isotherms. This is because the nanocrystalline (primary crystal) building blocks of SAPO-34-0.05 during the assembly and crystallization process have enlarged the mesopores and macropores between nanocrystalline[19]. The results of textural properties of SAPO-34 zeolites are shown in Supplementary Table 2.

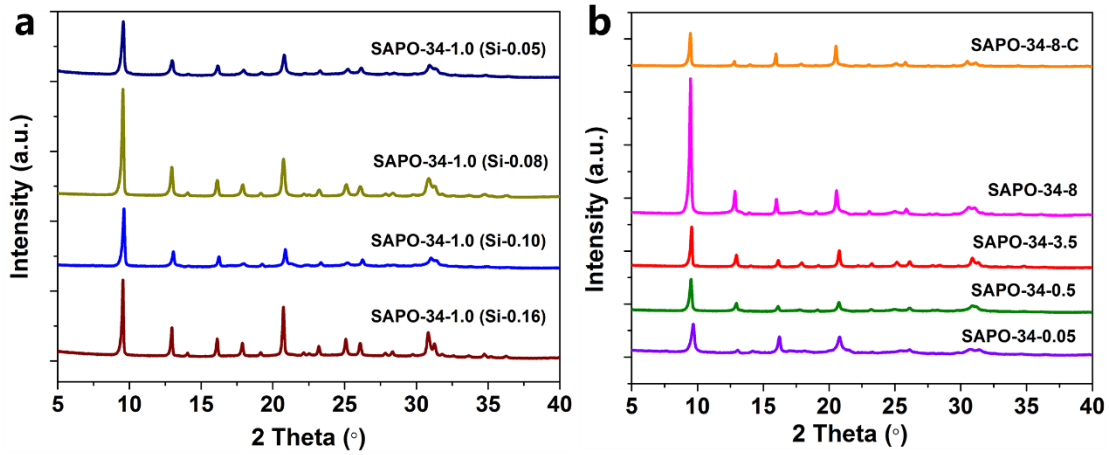

Supplementary Figure 2. XRD patterns of calcined SAPO-34 zeolites (**a**) with different Si content but similar crystal size and (**b**) with varying crystal size.

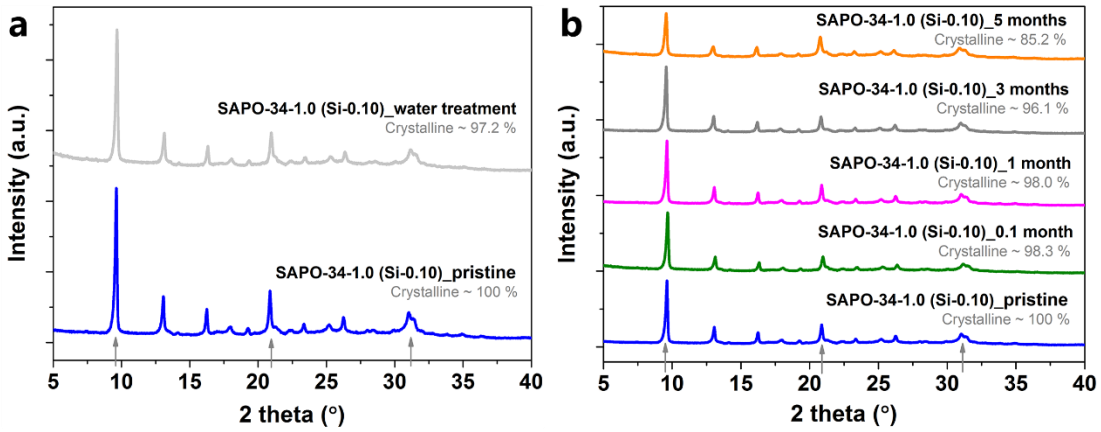

Supplementary Figure 3. XRD patterns of SAPO-34 zeolites (**a**) pre-adsorbed saturated water vapor and followed by outgassing and (**b**) exposed to air for different time.

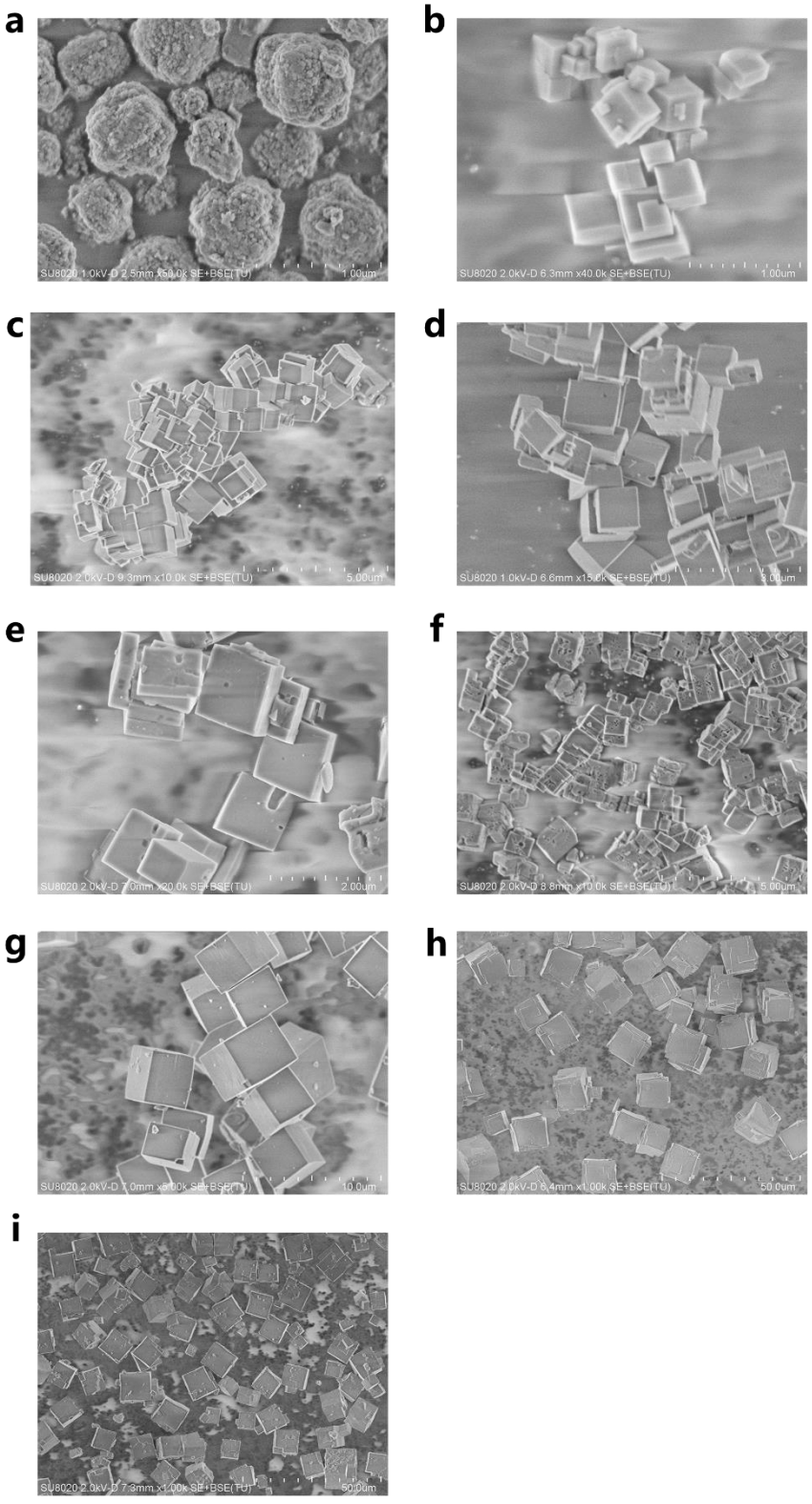

Supplementary Figure 4. FE-SEM images of SAPO-34 zeolites of (**a**) SAPO-34-0.05; (**b**) SAPO-34-0.5; (**c**) SAPO-34-1.0 (Si-0.16); (**d**) SAPO-34-1.0 (Si-0.10); (**e**) SAPO-34-1.0 (Si-0.08); (**f**) SAPO-34-1.0 (Si-0.05); (**g**) SAPO-34-3.5; (**h**) SAPO-34-8; (**i**) SAPO-34-8-C.

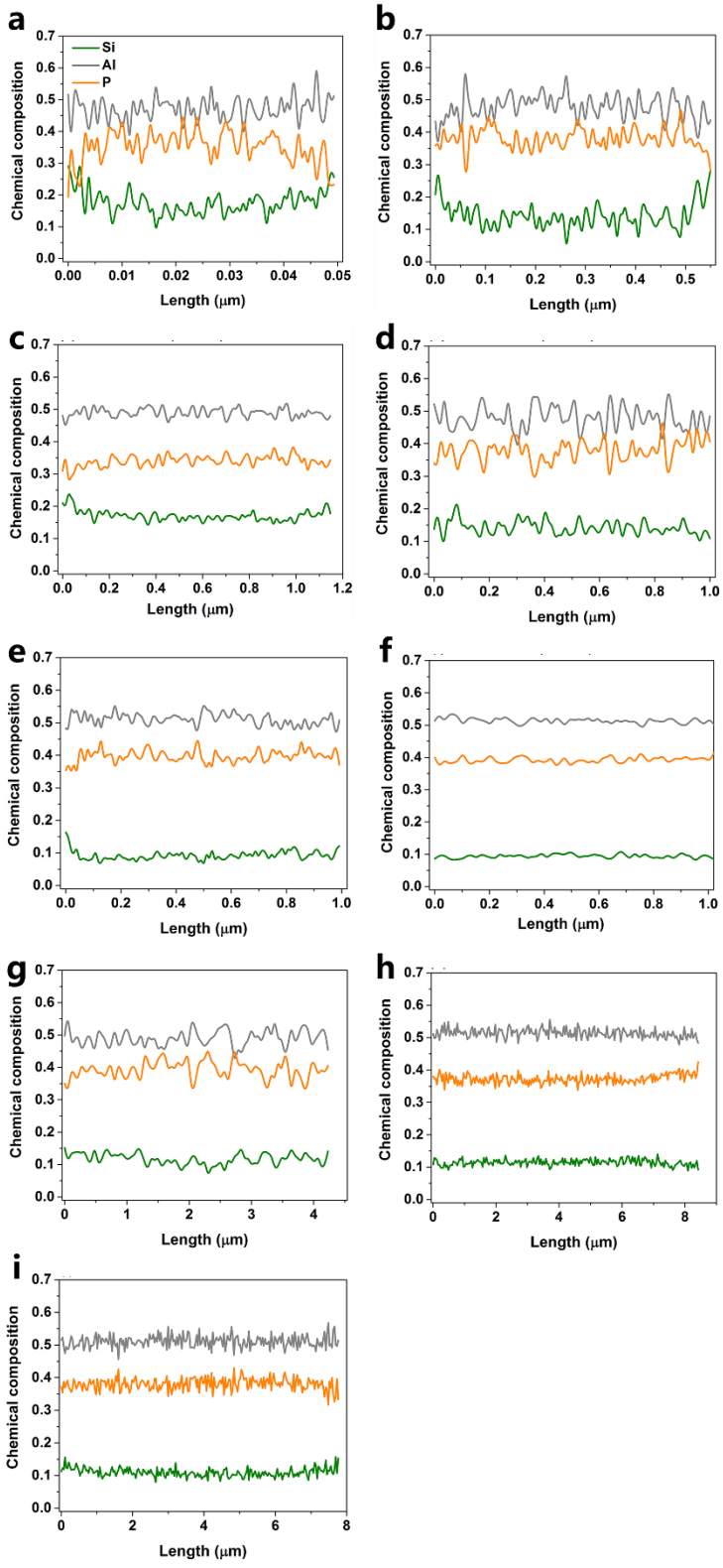

Supplementary Figure 5. The EDX analysis along the scan direction of SAPO-34 zeolites of (**a**) SAPO-34-0.05; (**b**) SAPO-34-0.5; (**c**) SAPO-34-1.0 (Si-0.16); (**d**) SAPO-34-1.0 (Si-0.10); (**e**) SAPO-34-1.0 (Si-0.08); (**f**) SAPO-34-1.0 (Si-0.05); (**g**) SAPO-34-3.5; (**h**) SAPO-34-8; (**i**) SAPO-34-8-C.

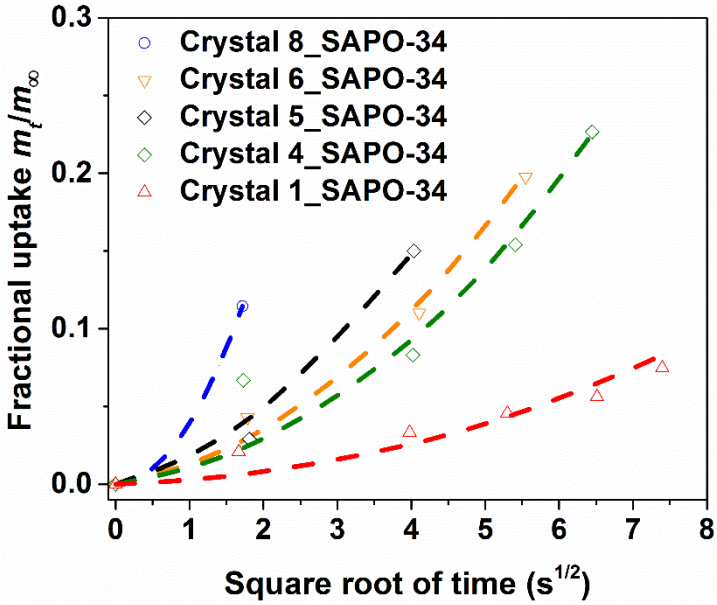

Supplementary Figure 6. The initial relative loading of methanol in single SAPO-34 zeolite crystal with square root of time at 298 K (0 → 1 mbar, ca. 0.57 $mmol_{MeOH}/g_{cat.}$). The dash lines represent the fitting results by equation (3), and the discrete points are uptake rate data by IFM technique reported by Remi et al.[7].

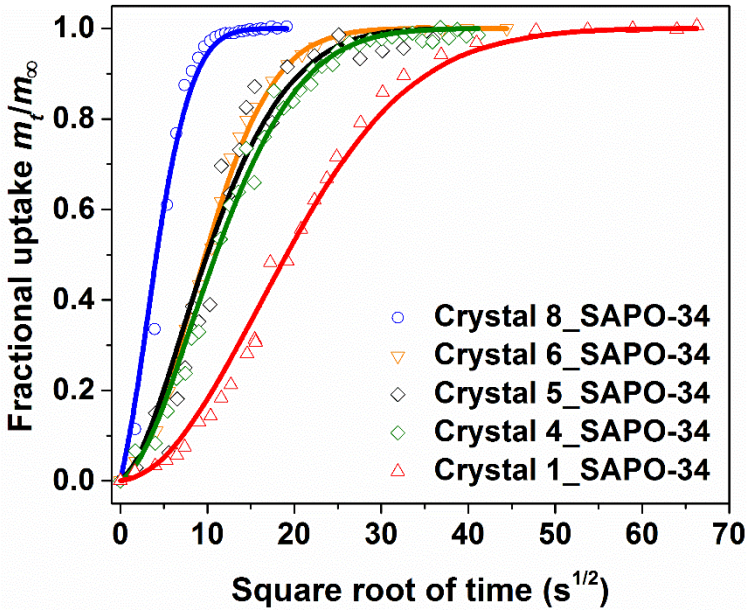

Supplementary Figure 7. The relative loading of methanol in single SAPO-34 zeolite crystal with square root of time at 298 K (0 → 1 mbar, ca. 0.57 $mmol_{MeOH}/g_{cat.}$). The solid lines represent the fitting results by equation (9), and the discrete points are uptake rate data by IFM technique reported by Remi et al.[7].

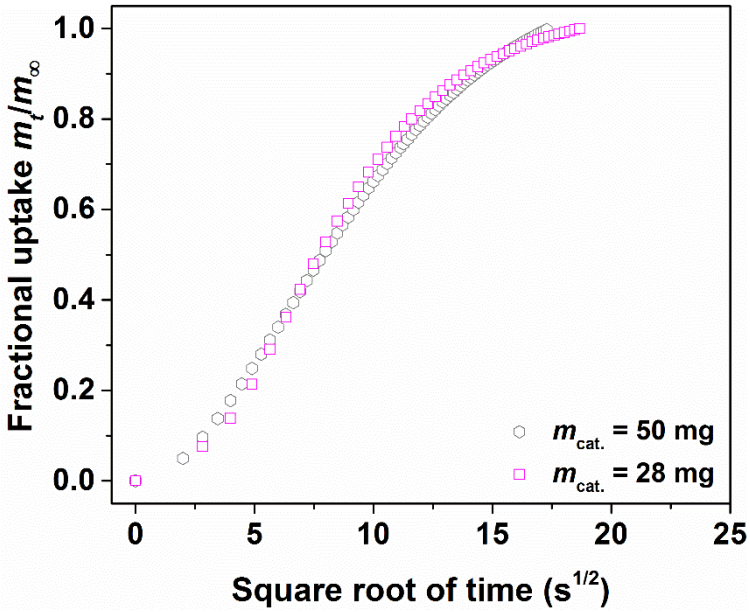

Supplementary Figure 8. Uptake rate measurement of methanol diffusion in SAPO-34 zeolites with different catalyst mass loading measured by IGA technique.

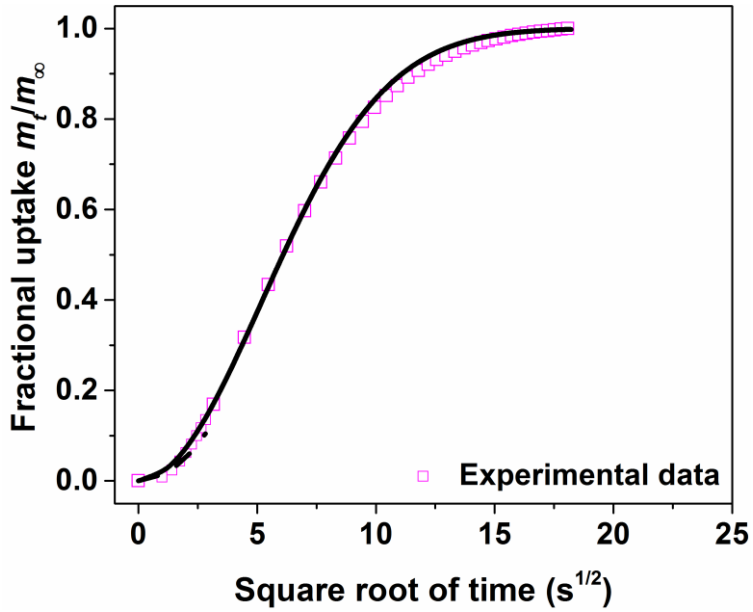

Supplementary Figure 9. The relative loading of methanol in SAPO-34 zeolites with square root of time at 303 K (0 → 0.6 mbar, ca. 0.41 $mmol_{MeOH}/g_{cat.}$). The solid line represents the fitting results by equation (9), the dash line represents the fitting results by equation (3), and the discrete points are uptake rate data measured by IGA technique.

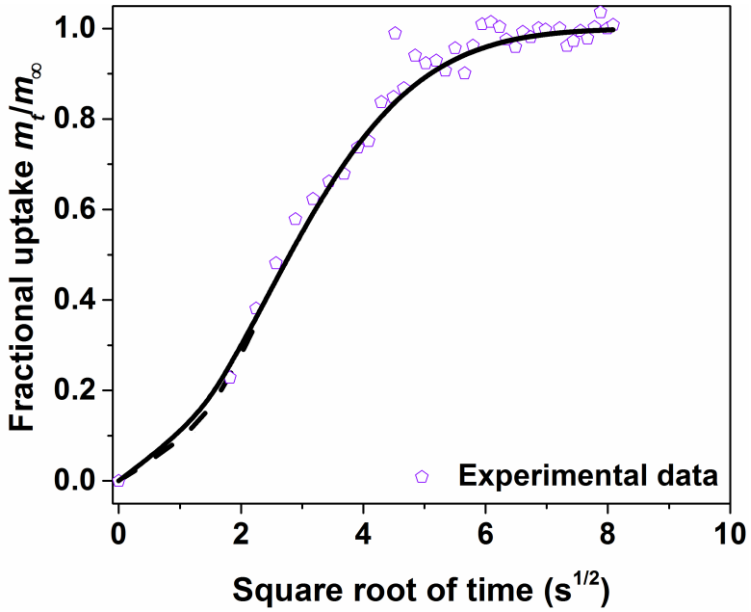

Supplementary Figure 10. The relative loading of methanol in SAPO-34 zeolites with square root of time at 303 K. The solid line represents the fitting results by equation (9), the dash line represents the fitting results by equation (3), and the discrete points are uptake rate data by TEOM technique from Chen et al.[11].

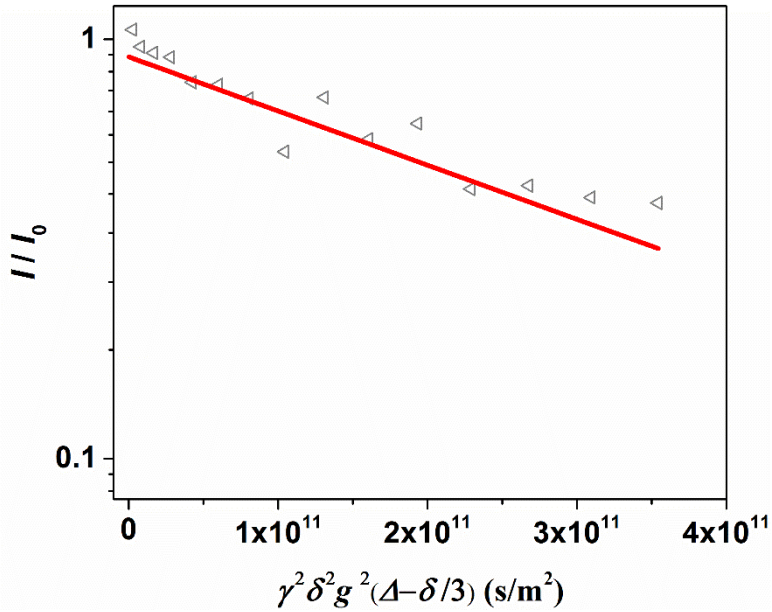

Supplementary Figure 11. The decay curve of ^{1}H PFG NMR spin-echo attenuation I/I_0 as a function of $\gamma^2\delta^2g^2(\Delta-\delta/3)$ for SAPO-34 zeolites loaded with 0.47 mmol/$g_{cat.}$ methanol at the temperature 303 K. Measurement conditions: gradient pulse duration δ = 1.3 ms, and diffusion time Δ = 10 ms. The solid line represents the fitting results by Supplementary Equation 30, and the discrete points are data measured by PFG NMR technique.

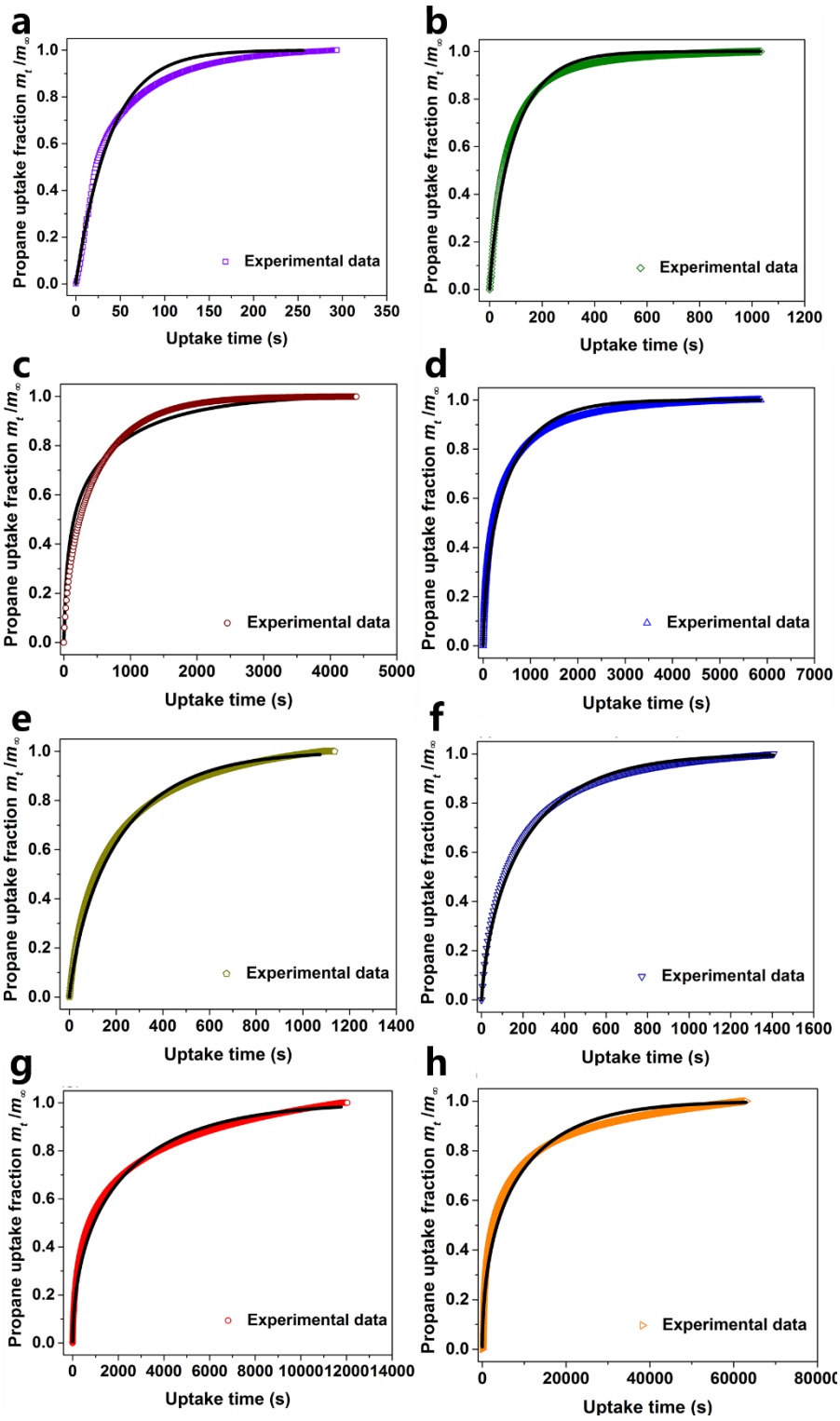

Supplementary Figure 12. Experimental propane uptake in pristine SAPO-34 zeolites of (**a**) SAPO-34-0.05; (**b**) SAPO-34-0.5; (**c**) SAPO-34-1.0 (Si-0.16); (**d**) SAPO-34-1.0 (Si-0.10); (**e**) SAPO-34-1.0 (Si-0.08); (**f**) SAPO-34-1.0 (Si-0.05); (**g**) SAPO-34-3.5; (**h**) SAPO-34-8 at 313 K (0 → 9 mbar). The solid line represents the fitting results by equation (9), and the discrete points are uptake rate data measured by IGA technique.

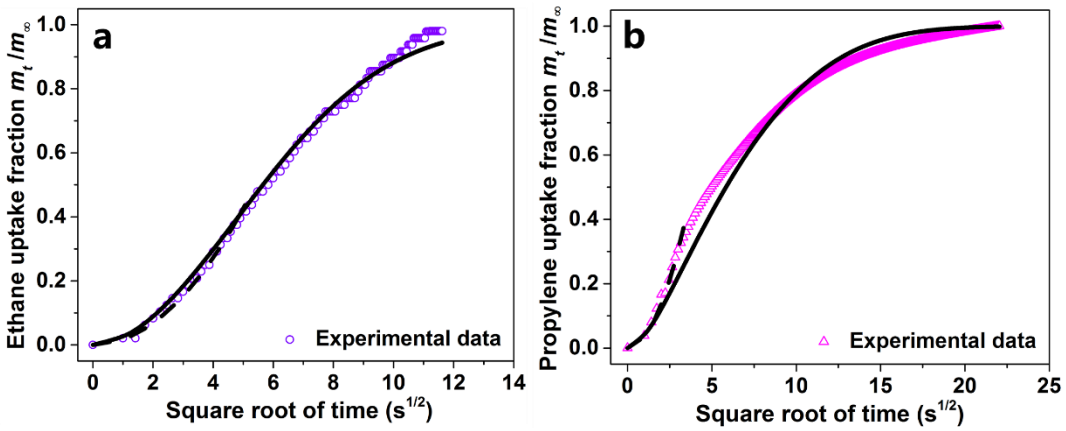

Supplementary Figure 13. The relative loading of (**a**) ethane and (**b**) propylene in SAPO-34 zeolites with 18 μm and 8 μm respectively at 313 K (0 → 10 mbar). The solid line represents the fitting results by equation (9), the dash line represents the fitting results by equation (3), and the discrete points are uptake rate data measured by IGA technique.

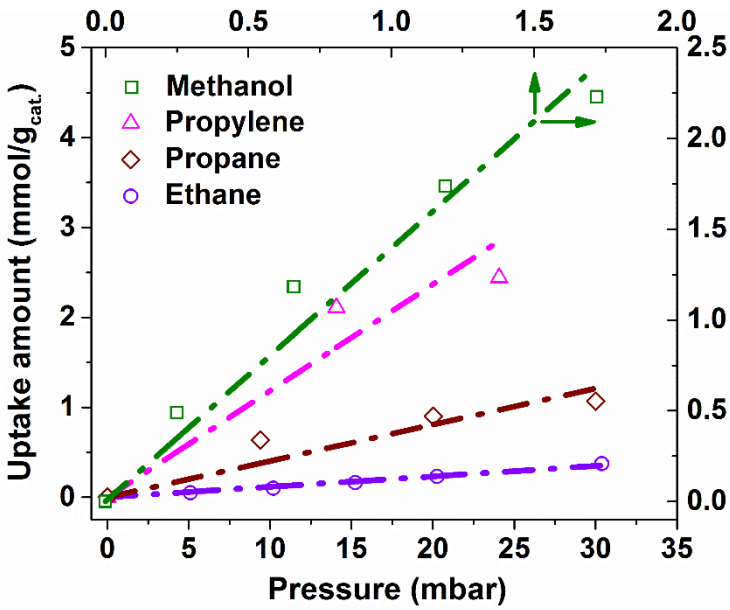

Supplementary Figure 14. The isothermal adsorption of methanol, propylene, propane and ethane in SAPO-34 zeolites at 313 K. The dash dot line represents the fitting results by Henry's law (Supplementary Equation 29) and the discrete points are experimental data measured by IGA technique. Up and right arrows indicate the data are based on up and right axes.

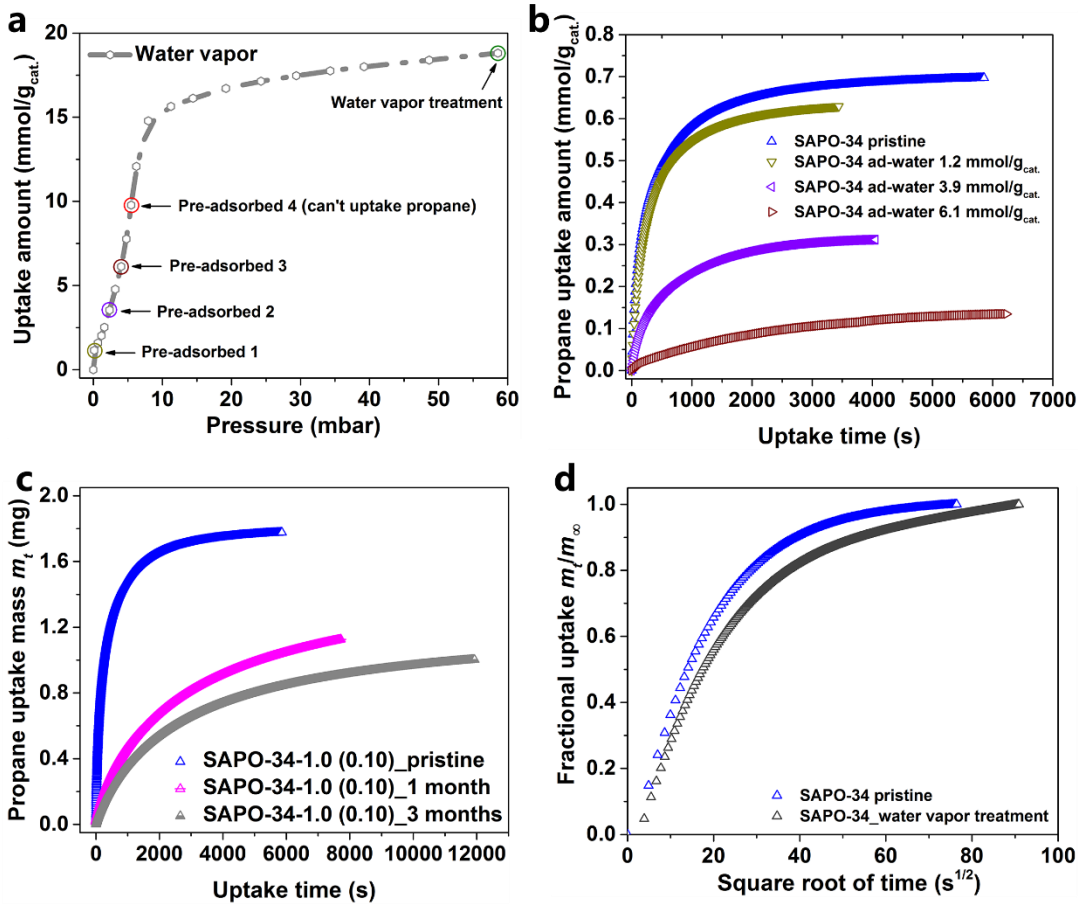

Supplementary Figure 15. (**a**) Adsorption isotherm of water on SAPO-34 zeolites at 313 K. Propane uptake measurement at 313 K (0 → 9 mbar) (**b**) in SAPO-34 zeolites with different quantity of adsorbed-water; (**c**) in SAPO-34 zeolites exposed to air for different time; (**d**) in SAPO-34 zeolites pre-adsorbed saturated water vapor at 313 K for 1 day and then outgassed at 623 K for 6 h. The discrete points are uptake rate data measured by IGA technique.

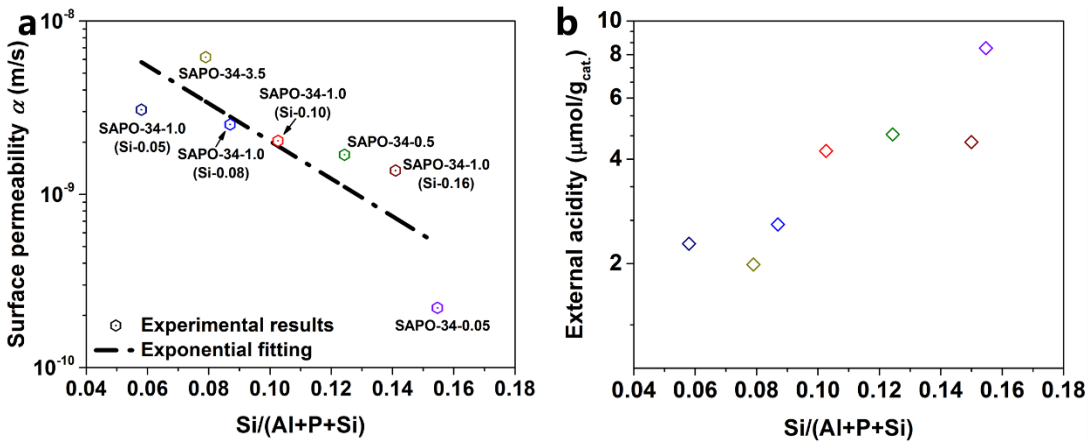

Supplementary Figure 16. (**a**)The correlation between surface permeability of propane at 313 K and Si content of pristine SAPO-34 zeolites; (**b**) the relation between Si content and external acidity of SAPO-34. An exponential function (dash dot line) is used to fit the relation between surface permeability and Si content of SAPO-34 zeolites.

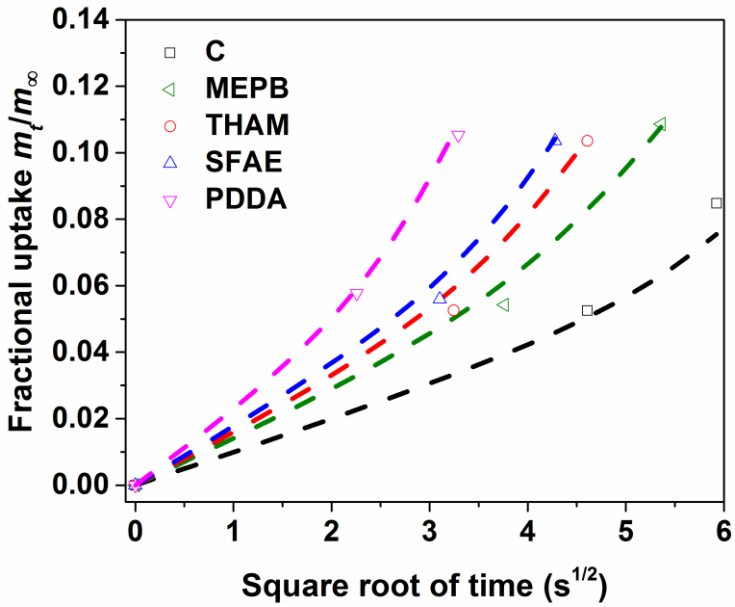

Supplementary Figure 17. The initial relative loading of 2-methylhexane in SAPO-11 hierarchical zeolites with square root of time at 288 K. The solid lines represent the fitting results by equation (3), and the discrete points are uptake rate data by IGA technique reported by Jin et al.[19].

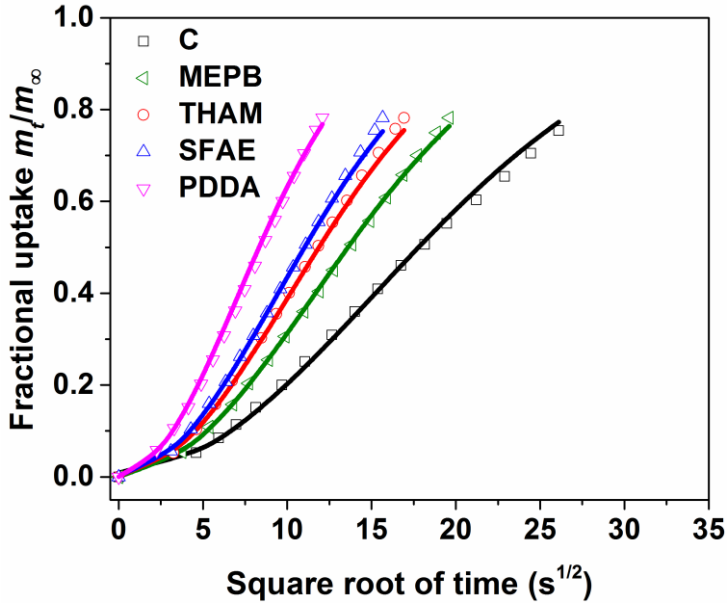

Supplementary Figure 18. The relative loading of 2-methylhexane in SAPO-11 hierarchical zeolites with square root of time at 288 K. The solid lines represent the fitting results by equation (1), and the discrete points are uptake rate data by IGA technique reported by Jin et al.[19].

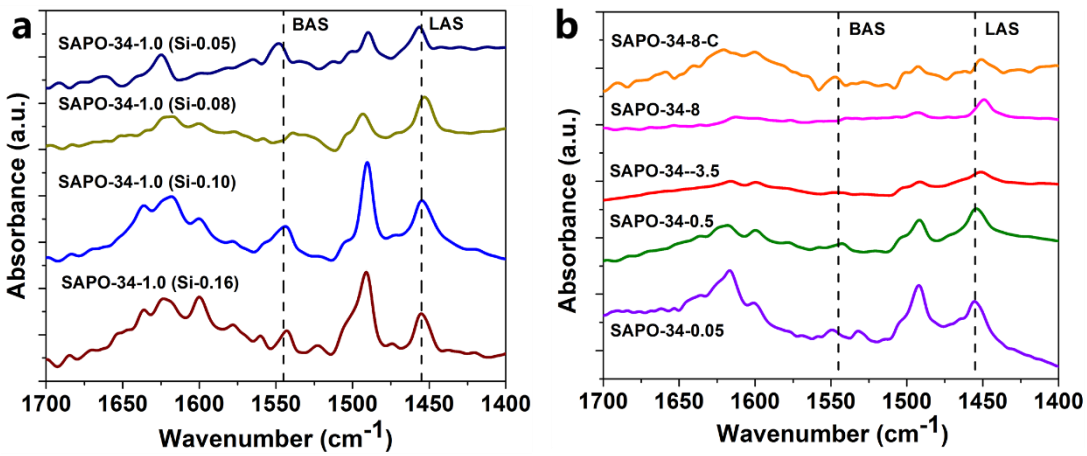

Supplementary Figure 19. FT-IR spectra of adsorbed pyridine on SAPO-34 zeolites at room temperature (**a**) with different Si content but similar crystal size and (**b**) with varying crystal sizes. The band at 1455 cm^{-1} corresponds to Lewis acid site (LAS). The band at 1545 cm^{-1} corresponds to Brønsted acid site (BAS).

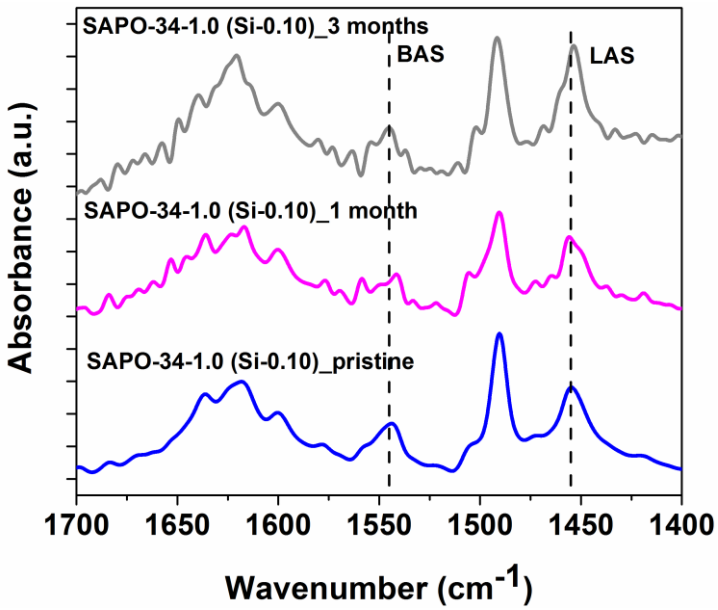

Supplementary Figure 20. FT-IR spectra of adsorbed pyridine on SAPO-34 zeolites at room temperature exposed to air for different time. The band at 1455 cm^{-1} corresponds to Lewis acid site (LAS). The band at 1545 cm^{-1} corresponds to Brønsted acid site (BAS).

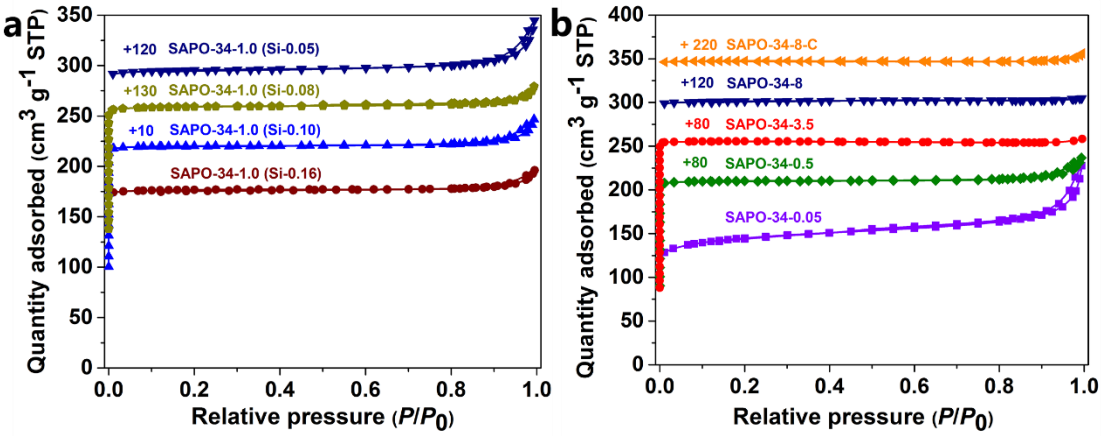

Supplementary Figure 21. N_2 adsorption and desorption isotherms at 77 K of the SAPO-34 zeolites (**a**) with different Si content but similar crystal size and (**b**) with varying crystal sizes.

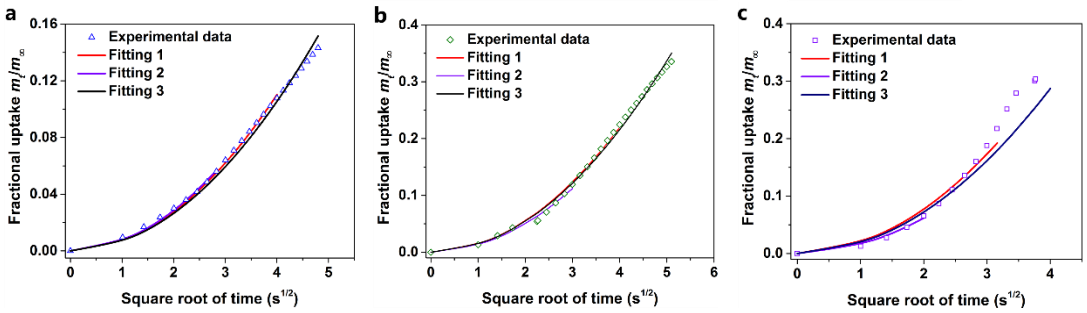

Supplementary Figure 22. The fitting results of equation (3) on the initial uptake stage with different uptake time interval.The uptake of propane in (**a**) SAPO-34-1.0 (Si-0.01), (**b**) SAPO-34-0.5, and (**c**) SAPO-34-0.05. Surface permeability (solid lines) was derived by equation (3).

Supplementary Table 1. Chemical composition of SAPO-34 zeolites by XRF

Sample	Integral composition
SAPO-34-0.05	$(Si_{0.155}Al_{0.421}P_{0.424})O_2$
SAPO-34-0.5	$(Si_{0.124}Al_{0.463}P_{0.413})O_2$
SAPO-34-0.1 (Si-0.16)	$(Si_{0.167}Al_{0.399}P_{0.434})O_2$
SAPO-34-0.1 (Si-0.10)	$(Si_{0.103}Al_{0.486}P_{0.412})O_2$
SAPO-34-0.1 (Si-0.10)_1 month	$(Si_{0.102}Al_{0.473}P_{0.425})O_2$
SAPO-34-0.1 (Si-0.10)_3 months	$(Si_{0.103}Al_{0.486}P_{0.412})O_2$
SAPO-34-0.1 (Si-0.08)	$(Si_{0.087}Al_{0.495}P_{0.420})O_2$
SAPO-34-0.1 (Si-0.05)	$(Si_{0.058}Al_{0.418}P_{0.524})O_2$
SAPO-34-3.5	$(Si_{0.079}Al_{0.492}P_{0.429})O_2$
SAPO-34-8	$(Si_{0.088}Al_{0.485}P_{0.428})O_2$
SAPO-34-8-C	$(Si_{0.084}Al_{0.477}P_{0.439})O_2$

Supplementary Table 2. Textural properties of SAPO-34 zeolites with varying crystal sizes by N_2 adsorption and desorption isotherms at 77 K

Sample	Surface area ($m^2/g_{cat.}$)		Pore Volume ($cm^3/g_{cat.}$)	
	S_{total}[a]	S_{micro}[b]	V_{total}[c]	V_{micro}[b]
SAPO-34-0.05	468.52	355.09	0.30	0.18
SAPO-34-0.5	432.05	421.95	0.22	0.20
SAPO-34-0.1 (Si-0.16)	557.17	544.40	0.29	0.27
SAPO-34-1.0 (Si-0.10)	543.34	526.03	0.28	0.26
SAPO-34-1.0 (Si-0.10)_1 month	535.43	515.11	0.28	0.25
SAPO-34-1.0 (Si0.10)_3 months	512.06	497.48	0.26	0.25
SAPO-34-1.0 (Si-0.08)	429.20	414.18	0.21	0.19
SAPO-34-0.1 (Si-0.05)	558.03	536.63	0.30	0.27
SAPO-34-3.5	581.56	578.29	0.27	0.27
SAPO-34-8	571.94	558.60	0.28	0.27
SAPO-34-8-C	404.15	399.07	0.21	0.21

[a] BET surface area determined from multipoint method. [b] S_{micro} (micropore area), S_{ext} (external surface area) and V_{micro} (micropore volume) determined from the t-plot method. [c] V_{total} (total volume) is determined from adsorbed volume at $P/P_0 = 0.98$.

Supplementary Table 3. External Lewis and Brønsted acidity of SAPO-34 zeolites with varying crystal size

Sample	Mass of wafer (mg)	Lewis acidity, 1450 cm^{-1} ($\mu mol/g_{cat.}$)	Brønsted acidity,1540 cm^{-1} ($\mu mol/g_{cat.}$)
SAPO-34-0.05	17.8	5.494	2.856
SAPO-34-0.5	18.3	3.672	1.042
SAPO-34-0.1 (Si-0.16)	17.4	2.821	1.655
SAPO-34-1.0 (Si-0.10)	20.8	1.586	1.986
SAPO-34-1.0 (Si-0.10)_1 month	13.6	2.382	1.840
SAPO-34-1.0 (Si-0.10)_3 months	20.2	3.208	1.573
SAPO-34-1.0 (Si-0.08)	16.1	2.348	0.247
SAPO-34-0.1 (Si-0.05)	17.9	1.267	1.015
SAPO-34-3.5	17.5	1.131	0.545
SAPO-34-8	21.6	1.805	0.184
SAPO-34-8-C	15.1	3.377	2.946

Supplementary Table 4. The surface permeability, intracrystalline diffusivity and effective diffusivity of methanol in SAPO-34 zeolites measured by different techniques and determined by our proposed method (diffusional activation energy E_a = 25.30 kJ/mol)

Measured techniques (measured temperature K)		Surface permeability α (m/s)	Intracrystalline diffusivity D (m^2/s)	Effective diffusivity D_{eff} (m^2/s) [a]	R^2 [b]
IFM [c] (298 K)	Crystal 1	1.61×10^{-8}	5.75×10^{-13}	5.19×10^{-14}	0.9926
	Crystal 4	6.49×10^{-8}	8.15×10^{-13}	1.97×10^{-13}	0.9932
	Crystal 5	1.11×10^{-7}	5.75×10^{-13}	2.51×10^{-13}	0.9530
	Crystal 6	8.14×10^{-8}	1.70×10^{-12}	2.83×10^{-13}	0.9975
	Crystal 8	5.27×10^{-7}	1.22×10^{-12}	8.07×10^{-13}	0.9841
	Average	1.60×10^{-7}	9.77×10^{-13}	3.18×10^{-13}	0.9841
IGA [d] (303 K)		2.57×10^{-8}	9.71×10^{-13}	1.66×10^{-14}	0.9977
TEOM [e] (303 K)		2.99×10^{-8}	1.05×10^{-12}	5.79×10^{-15}	0.9782
PFG NMR (303 K)		-	$(2.55 \pm 1.01) \times 10^{-12}$	-	0.8894

[a] The effective diffusivity is calculated by equation (7). [b] Fitting efficiency of equation (9) (Supplementary Equation 30 for PFG NMR), coefficient of determination of analytical DRM expression on uptake curve. [c] The original uptake rate data were obtained by IFM technique from Remi et al. [7]; [d] the uptake rate by IGA technique were carried out in our laboratory; [e] the original uptake rate data were obtained by TEOM technique from Chen et al. [11]; [f] the diffusion of methanol by PFG NMR technique were carried out in our laboratory.

Supplementary Table 5. The surface permeability, intracrystalline diffusivity and effective diffusivity of propane in SAPO-34 zeolites with varying crystal size and Si content at 313 K

Sample	α (m/s)	D (m^2/s)	D_{eff} (m^2/s) [a]	$L = \alpha l/D$	R^2 [b]
SAPO-34-0.05	2.21×10^{-10}	1.05×10^{-16}	8.99×10^{-19}	0.03	0.9810
SAPO-34-0.5	1.69×10^{-9}	1.25×10^{-16}	2.82×10^{-17}	1.67	0.9873
SAPO-34-1.0 (0.16)	1.37×10^{-9}	8.66×10^{-17}	5.84×10^{-17}	6.19	0.9620
SAPO-34-1.0 (0.10)	2.03×10^{-9}	7.50×10^{-17}	5.17×10^{-17}	6.67	0.9800
SAPO-34-1.0 (0.08)	2.53×10^{-9}	2.35×10^{-16}	1.10×10^{-16}	2.65	0.9980
SAPO-34-1.0 (0.05)	3.07×10^{-9}	1.98×10^{-16}	1.11×10^{-16}	3.82	0.9960
SAPO-34-3.5	6.18×10^{-9}	1.23×10^{-16}	1.15×10^{-16}	43.30	0.9842
SAPO-34-8	5.74×10^{-9}	1.63×10^{-16}	1.56×10^{-16}	69.39	0.9600

[a] The effective diffusivity is calculated by equation (7). [b] Fitting efficiency of equation (9), coefficient of determination of analytical DRM expression on uptake curve.

Supplementary Table 6. The Henry's constant, surface permeability and intracrystalline diffusivity of methanol, ethane, propylene and propane in SAPO-34 zeolites at 313 K

Guest	K (mol·bar^{-1}·$g_{cat.}^{-1}$)	α (m/s)	D (m^2/s)	$L = \alpha l/D$
Methanol	1.3956	2.57×10^{-8}	9.71×10^{-13}	0.0522
Ethane	0.0116	7.56×10^{-8}	1.25×10^{-12}	0.5442
Propylene	0.1183	6.69×10^{-8}	3.35×10^{-14}	7.9874
Propane	0.0403	5.74×10^{-9}	1.56×10^{-16}	69.3900

Supplementary Table 7. The surface permeability, intracrystalline diffusivity and effective diffusivity of propane at 313 K in SAPO-34 zeolites treated by water vapor at 313 K and exposed to air (298 K) for different time

Sample	α (m/s)	D (m^2/s)	D_{eff} (m^2/s) [a]	$L = \alpha l/D$	R^2 [b]
SAPO-34-1.0 (Si-0.10) [c]	2.03×10^{-9}	7.50×10^{-17}	5.17×10^{-17}	6.67	0.9800
SAPO-34-1.0 (Si-0.10)_0.1 month [d]	1.12×10^{-9}	6.50×10^{-17}	3.51×10^{-17}	4.82	0.9812
SAPO-34-1.0 (Si-0.10)_1 month [d]	1.78×10^{-10}	4.50×10^{-17}	1.10×10^{-17}	0.97	0.9941
SAPO-34-1.0 (Si-0.10)_3 months [d]	1.45×10^{-10}	2.19×10^{-17}	7.71×10^{-18}	1.63	0.9981
SAPO-34-1.0 (Si-0.10)_5 month [d]	1.33×10^{-10}	1.67×10^{-17}	7.47×10^{-18}	2.43	0.9982
SAPO-34-1.0 (Si-0.10)_water treatment [e]	1.33×10^{-9}	5.10×10^{-17}	3.48×10^{-17}	6.39	0.9747

[a] The effective diffusivity is calculated by equation (7). [b] Fitting efficiency of equation (9), coefficient of determination of analytical DRM expression on uptake curve; [c] After removing the template of sample by calcination; [d] After removing the template of sample by calcination, then the sample was stored in humid air for 0.1, 1, 3 or 5 months; [e] The sample was pre-adsorbed water vapor at 60 mbar (~ saturated vapor pressure) under 313 K for 1 day. Before the uptake rate measurements, the samples were outgassed at 623 K at least 6 h.

Supplementary Table 8. The surface permeability of propane at 313 K in SAPO-34 zeolites pre-adsorbed different quantity of water

Sample	α (m/s)	R^2 [a]
SAPO-34-1.0 (Si-0.10)_water ad_1 [b]	1.40×10^{-9}	0.9896
SAPO-34-1.0 (Si-0.10)_water ad_2 [b]	7.43×10^{-10}	0.9977
SAPO-34-1.0 (Si-0.10)_water ad_3 [b]	2.38×10^{-10}	0.9800
SAPO-34-1.0 (Si-0.10)_water ad_4 [b]	can't uptake	-

[a] Fitting efficiency of equation (3); [b] The sample was pre-adsorbed water vapor with 1.2 (index: 1), 3.9 (index: 2), 6.1 (index: 3) and 9.2 (index: 4) mmol/$g_{cat.}$ under 313 K for 1 h, then without outgassing the sample, the uptake rate measurement was performed.

Supplementary Table 9. The reciprocal of characteristic time of surface barriers, intracrystalline diffusion, overall mass transfer of 2-methylhexane in SAPO-11 hierarchical materials with diverse crystal morphologies at 288 K determined by our proposed method [a]

Growth modifiers [b]	α/l (s^{-1})	D/l^2 (s^{-1})	D_{eff}/l^2 (s^{-1}) [c]	R^2 [d]
PDDA	1.00×10^{-2}	1.59	4.75×10^{-3}	0.9972
SFAE	5.69×10^{-3}	1.08	2.84×10^{-3}	0.9979
THAM	4.90×10^{-3}	0.93	2.40×10^{-3}	0.9977
MEPB	3.75×10^{-3}	1.21	1.80×10^{-3}	0.9992
C (without)	2.15×10^{-3}	1.55	8.90×10^{-4}	0.9968

[a] The original uptake rate data were obtained by IGA from Jin et al. [19]; [b] using different growth modifier could alter morphology of SAPO-11 hierarchical materials [19]. [c] Jin et al.[19] reported in their research. [d] Fitting efficiency, coefficient of determination of analytical DRM expression on uptake curve.

Supplementary Table 10. The fitting results of intracrystalline diffusivity by DRM with obtained surface permeability from the equation (3), based on the uptake of propane in SAPO-34-1.0 (Si-0.10), SAPO-34-0.5 and SAPO-34-0.05.

Sample	Fitting	α_0 (m/s) [a]	D (m^2/s) [b]	R^2 [c]
SAPO-34-1.0	Fitting 1	2.03×10^{-9}	7.50×10^{-17}	0.980
(Si-0.10)	Fitting 2	2.10×10^{-9}	7.38×10^{-17}	0.978
	Fitting 3	1.95×10^{-9}	7.50×10^{-17}	0.976
SAPO-34-0.5	Fitting 1	1.69×10^{-9}	1.25×10^{-16}	0.987
	Fitting 2	1.53×10^{-9}	1.45×10^{-16}	0.985
	Fitting 3	1.66×10^{-9}	1.35×10^{-16}	0.985
SAPO-34-0.05	Fitting 1	2.21×10^{-10}	1.05×10^{-16}	0.981
	Fitting 2	2.37×10^{-10}	2.00×10^{-16}	0.972
	Fitting 3	1.90×10^{-10}	1.31×10^{-16}	0.973

[a] Initial value of surface permeability determined by the equation (3) as shown in Supplementary Figure 22. [b] Fitting results of DRM with obtained surface permeability. [c] Fitting efficiency of DRM.

Supplementary Table 11. The fitting results of intracrystalline diffusivity and characteristic factor *L* by DRM with two free fitting parameters, based on the uptake of propane in SAPO-34-1.0 (Si-0.10).

D_0 (m^2/s) [a]	L_0 [a]	D (m^2/s) [b]	L [b]	R^2 [c]
7.50×10^{-16}	1	7.36×10^{-16}	1.18	0.965
7.50×10^{-16}	0.01	4.60×10^{-15}	0.051	0.960
7.50×10^{-15}	0.01	1.16×10^{-14}	0.020	0.950
7.50×10^{-14}	0.01	1.70×10^{-14}	0.014	0.950

[a] Initial fitting values for DRM. [b] Fitting results of DRM with correspond initial values. [c] Fitting efficiency of DRM.

Supplementary References

1. Titze, T. *et al.* Transport in Nanoporous Materials Including MOFs: The Applicability of Fick's Laws. *Angew. Chem. Int. Ed.* **54**, 14580-14583 (2015).

2. Kärger, J., Ruthven, D. M. & Theodorou, D. N. *Diffusion in Nanoporous Materials* (Wiley-VCH, Weinheim, 2012).

3. Crank, J. *The mathematics of diffusion* (Oxford university press, London, 1979).

4. Humplik, T., Raj, R., Maroo, S. C., Laoui, T. & Wang, E. N. Effect of Hydrophilic Defects on Water Transport in MFI Zeolites. *Langmuir* **30**, 6446-6453 (2014).

5. Chen, D., Rebo, H. P. & Holmen, A. Diffusion and deactivation during methanol conversion over SAPO-34: a percolation approach. *Chem. Eng. Sci.* **54**, 3465-3473 (1999).

6. Heinke, L. Significance of concentration-dependent intracrystalline diffusion and surface permeation for overall mass transfer. *Diffus. Fundam.* **4**, 12.11-12.11 (2007).

7. Remi, J. C. S. *et al.* The role of crystal diversity in understanding mass transfer in nanoporous materials. *Nat. Mater.* **15**, 401-406 (2016).

8. Gao, B. *et al.* A low-temperature approach to synthesize low-silica SAPO-34 nanocrystals and their application in the methanol-to-olefins (MTO) reaction. *Catal. Sci. Technol.* **6**, 7569-7578 (2016).

9. Yang, M. *et al.* A top-down approach to prepare silicoaluminophosphate molecular sieve nanocrystals with improved catalytic activity. *Chem. Commun.* **50**, 1845-1847 (2014).

10. Wu, P. *et al.* Synthesis of nanosized SAPO-34 with the assistance of bifunctional amine and seeds. *Chem. Commun.* **54**, 11160-11163 (2018).

11. Chen, D., Rebo, H. P., Moljord, K. & Holmen, A. Methanol Conversion to Light Olefins over SAPO-34. Sorption, Diffusion, and Catalytic Reactions. *Ind. Eng. Chem. Res.* **38**, 4241-4249 (1999).

12. Tanaka, S. *et al.* Adsorption and Diffusion Phenomena in Crystal Size Engineered ZIF-8 MOF. *J. Phys. Chem. C* **119**, 28430-28439 (2015).

13. Kärger, J. Transport Phenomena in Nanoporous Materials. *ChemPhysChem* **16**, 24-51 (2015).

14. Chmelik, C. *et al.* Mass Transfer in a Nanoscale Material Enhanced by an Opposing Flux. *Phys. Rev. Lett.* **104**, 085902 (2010).

15. Beerdsen, E., Dubbeldam, D. & Smit, B. Understanding Diffusion in Nanoporous Materials.

Phys. Rev. Lett. **96**, 044501 (2006).

16. Wang, C. *et al.* Dual template-directed synthesis of SAPO-34 nanosheet assemblies with improved stability in the methanol to olefins reaction. *J. Mater. Chem. A* **3**, 5608-5616 (2015).

17. Yarulina, I. *et al.* Structure–performance descriptors and the role of Lewis acidity in the methanol-to-propylene process. *Nat. Chem.* **10**, 804-812 (2018).

18. Emeis, C. A. Determination of Integrated Molar Extinction Coefficients for Infrared Absorption Bands of Pyridine Adsorbed on Solid Acid Catalysts. *J. Catal.* **141**, 347-354 (1993).

19. Jin, D. *et al.* Hierarchical Silicoaluminophosphate Catalysts with Enhanced Hydroisomerization Selectivity by Directing the Orientated Assembly of Premanufactured Building Blocks. *ACS Catal.* **7**, 5887-5902 (2017).